

Surface Defect Detection via Entity Sparsity Pursuit With Intrinsic Priors

Jianzhu Wang , Qingyong Li , *Member, IEEE*, Jinrui Gan , Haomin Yu, and Xi Yang

Abstract—Computer vision based methods have been widely used in surface defect inspection. However, most of these approaches are task specific, and it is hard to transfer them to similar detection scenarios. This paper proposes an entity sparsity pursuit (ESP) method to identify surface defects. Based on the observation that surface image textures usually form a low-rank structure and the structure can be violated by the presence of rare defects, we formulate the detection task as a low-rank and ESP problem. To alleviate the feature shortage issue existed in industrial gray-scale images, we customize a kind of intuitive features for surface defect inspection. Different from previous work utilizing complicated regularization terms, we resort to mine intrinsic priors of defect images, which can be neatly incorporated into the designed architecture. The proposed model is compact and able to detect surface defects in an unsupervised manner. To fully evaluate the presented method, we conduct a series of experiments using three real-world and one synthetic defect datasets. Experimental results demonstrate that ESP outperforms state-of-the-art methods.

Index Terms—Entity sparsity, feature extraction, intrinsic prior, surface defect detection.

I. INTRODUCTION

SURFACE defect detection is a critical step in many industrial applications. With the requirements of high-quality inspection, advanced computer vision technologies have evolved into a mainstream and replaced conventional manual inspection, which suffers from both low efficiency and high labor intensity.

Surface defects in industry are generally defined as local anomalies embedded in homogeneous textures. In order to

Manuscript received January 28, 2019; revised April 23, 2019; accepted May 7, 2019. Date of publication May 17, 2019; date of current version January 4, 2020. This work was supported in part by the Fundamental Research Funds for the Central Universities under Grant 2018YJS042 and Grant 2016JBZ006, in part by the Open Fund of Beijing Intelligent Logistics System Collaborative Innovation Center under Grant 2018KF-07, and in part by Shanghai Research Program under Grant 17511102900. Paper no. TII-19-0307. (*Corresponding author: Qingyong Li.*)

J. Wang, Q. Li, and H. Yu are with the Beijing Key Laboratory of Transportation Data Analysis and Mining, Beijing Jiaotong University, Beijing 100044, China (e-mail: jzwang@bjtu.edu.cn; liqy@bjtu.edu.cn; 17112085@bjtu.edu.cn).

J. Gan is with Global Energy Interconnection Research Institute Company, Ltd., Beijing 102209, China (e-mail: 15112103@bjtu.edu.cn).

X. Yang is with the School of Information, Beijing Wuzi University, Beijing 101149, China (e-mail: yxyoung@163.com).

Color versions of one or more of the figures in this paper are available online at <http://ieeexplore.ieee.org>.

Digital Object Identifier 10.1109/TII.2019.2917522

enable automatic and nondestructive detection, visual inspection systems (VISs) have found wide applications in surface inspection of steel [1], tire [2], rail [3], solar modules [4], printed circuit boards [5], and other planar products [6]. Noted that the majority of existing VIS are designed to detect defects in specific scenarios, and the generalization capability of these approaches is thus constrained. In general, these inspection techniques can be roughly divided into three categories: spectral, statistical, and model-based methods. The basic idea of spectral approaches is to transform images to frequency domain, where responses of defects and faultless background are expected to be different and thus defects can be identified. Obviously, such methods are appropriate for surfaces appearing regular patterns and periodic textures such as fabrics [7], but the selection of filters can affect their performance to some extent. Statistical approaches usually employ co-occurrence matrix [8], histogram [9], and other texture statistics to detect surface defects. Unfortunately, both spectral and statistical methods can hardly deal with the situation where stochastic variations appeared in randomly textured surfaces [10]. To this end, Xie and Mirmehdi [11] presented texture exemplars for detecting and localizing defects in random color textures. Based on the Markov random field model, a supervised method [12] was developed to monitor and diagnose stochastic textured surfaces. Typically, model-based approaches tend to require a high computational complexity [13].

Recently, fine-designed deep convolutional neural networks have emerged as powerful tools in a variety of computer vision tasks. As a result, several studies have attempted to use deep learning (DL) methods for defect inspection [14], [15], but these methods still face great challenges. As mentioned in [16], training a DL model usually requires considerable samples while collecting and labeling a large number of defect images could be costly. Furthermore, DL approaches depend on the dataset with specific supervision information; thus, the learned model is coupled tightly with a certain dataset and may not perform well on other datasets.

Considering the factors mentioned above, we aim to propose a more general vision architecture for surface defect detection. In terms of feature extraction, we design an intuitive local binary pattern (LBP) inspired feature extractor, which is applicable to surface defect inspection scenarios. From the perspective of model construction, customized regularization terms are abandoned in the underlying algorithm and thus a compact model is retained. The main contributions of this paper are summarized as follows.

- 1) We propose to detect surface defects at the entity level rather than pixel level, and thus the sparseness of the defect is better characterized.
- 2) We provide a paradigm of incorporating intrinsic priors of defect images, which enables the designed model to resist noise interference and achieve parameter robustness.
- 3) We introduce a framework for VIS in industrial applications, which offers a good generalization ability for different detection tasks.

The remainder of this paper is organized as follows. We review some preliminaries in Section II. Section III details the proposed method. In Section IV, experiments on three real-world and one synthetic surface defect datasets are conducted and analyzed. Section V concludes this paper.

II. PRELIMINARIES

As a widely used technique for data analysis and dimension reduction, principal component analysis (PCA) always supposes that noise in data follows a Gaussian distribution, i.e., classical PCA is incapable of handling the data corrupted by anomalies with large magnitudes. Therefore, robust PCA (RPCA) [17] was proposed to tackle this problem. It considers decomposing the observed data matrix X into a low-rank matrix L and a sparse matrix E corresponding to the intact data and the corruptions, respectively. The optimization problem is

$$\begin{aligned} \min_{L,E} \quad & \text{rank}(L) + \lambda \|E\|_0 \\ \text{s.t.} \quad & X = L + E \end{aligned} \quad (1)$$

where $\text{rank}(L)$ denotes the rank of matrix L , $\|E\|_0$ represents the ℓ_0 norm of matrix E , i.e., the number of nonzero elements in E , and $\lambda > 0$ is a parameter that trades off the rank of L versus the sparsity of E . However, the above problem is nonconvex and thus intractable. To mitigate this problem, Candès *et al.* [17] show that under rather weak assumptions, it can be relaxed to the following convex problem:

$$\begin{aligned} \min_{L,E} \quad & \|L\|_* + \lambda \|E\|_1 \\ \text{s.t.} \quad & X = L + E \end{aligned} \quad (2)$$

where $\|\cdot\|_*$ is the nuclear norm, i.e., sum of singular values, and $\|\cdot\|_1$ means the ℓ_1 norm, which sums the absolute values of all entries in a matrix.

Different from RPCA, low-rank representation (LRR) assumes that the data are derived from multiple subspaces [18]. It is more applicable for defect detection scenarios due to the mixed nature of the image data. LRR solves the following optimization problem:

$$\begin{aligned} \min_{Z,E} \quad & \|Z\|_* + \lambda \|E\|_{2,1} \\ \text{s.t.} \quad & X = DZ + E \end{aligned} \quad (3)$$

where the minimizer Z denotes the reconstruction coefficients of X with respect to the dictionary D , and the residue E is constrained with the $\ell_{2,1}$ norm, which is defined as the sum of

ℓ_2 norms of the columns in a matrix

$$\|E\|_{2,1} = \sum_i \sqrt{\sum_j (E(j,i))^2} \quad (4)$$

where $E(j,i)$ represents the (j,i) th entry of E . If the dictionary D is set as the identity matrix, LRR could be regarded as a generalization of RPCA. By directly choosing X as the dictionary matrix as suggested in [18], we have the following convex optimization problem:

$$\begin{aligned} \min_{Z,E} \quad & \|Z\|_* + \lambda \|E\|_{2,1} \\ \text{s.t.} \quad & X = XZ + E. \end{aligned} \quad (5)$$

Apparently, the $\ell_{2,1}$ norm encourages E to have sparse columns. It explicitly assumes that the corruptions in data are “sample specific,” i.e., some data vectors are corrupted and the others are clean [19].

III. PROPOSED METHOD

Fig. 1 presents the overall framework of the proposed method, and the critical steps are elaborated in the following sections.

A. Image Preprocessing

To partly reduce the impacts of illumination inequality or other unfavorable factors, we preprocess defect images using logarithm transformation and Gamma correction. These operations are expected to smooth background of original images, and one sample image can be found in Fig. 1.

B. Feature Extraction

Discriminative features are crucial in terms of low-rank-based anomaly detection. In order to detect salient object more accurately, Shen and Wu [20] proposed a classical feature combination, in which features including color, steerable pyramids, and Gabor filters were extracted to form a 53-dimensional (53-D) feature vector. However, simply using high-dimensional features might have a negative influence on the dissimilarity measurement of defects and background. More importantly, such a high dimensionality may result in unacceptable computational burden for subsequent matrix operations. To alleviate this issue, we utilize the following feature extractors.

First, we customize a kind of LBP-inspired feature extractor, which is tailored for surface inspection scenarios. To make it clear, we briefly review the concept of LBP [21]. As a feature extractor, LBP is invented to depict the local texture of an image. For a given pixel in the image, an LBP code is calculated by comparing it with its neighbors

$$\text{LBP}_{neN,neR} = \sum_{k=0}^{neN-1} \Phi(g_k - g_c) 2^k, \Phi(x) = \begin{cases} 1, & x \geq 0 \\ 0, & x < 0 \end{cases} \quad (6)$$

where g_c is the gray value of the central pixel, g_k signifies the value of its neighbors, neN indicates the total number of involved neighbors, and neR denotes the radius of the neighborhood. Furthermore, the rotation invariant LBP can be defined as

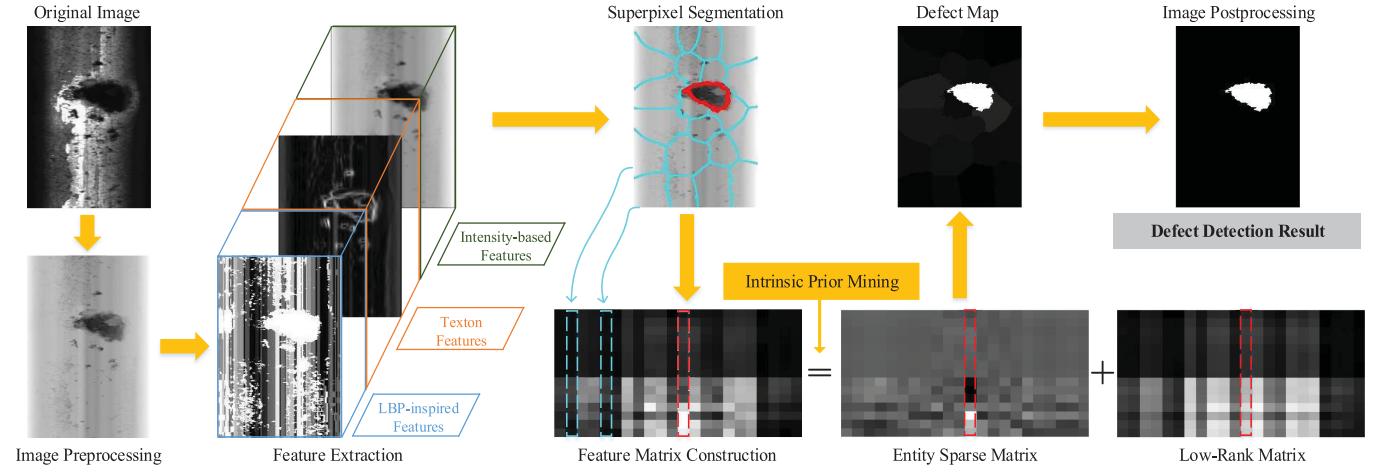


Fig. 1. Framework of the proposed method.

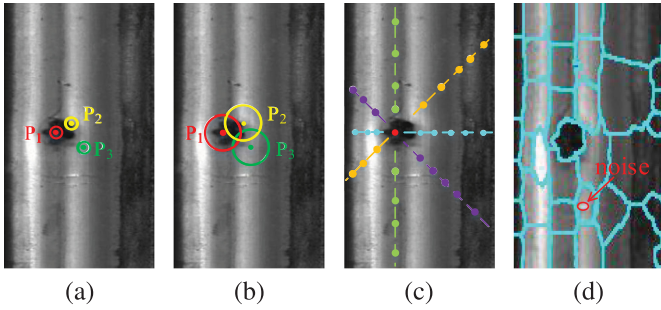


Fig. 2. (a) LBP operator with a small radius. (b) LBP operator with a large radius. (c) LBP-inspired feature extractor. (d) Superpixel segmentation result. For visualization, the rail image is not preprocessed.

follows:

$$\text{LBP}_{neN, neR}^{\text{ri}} = \min \{ \text{ROR}(\text{lbp}, \beta) | \beta = 0, 1, \dots, neN - 1 \} \quad (7)$$

where lbp equals to (6), ri stands for rotation invariance, and $\text{ROR}(\text{lbp}, \beta)$ performs β times circular bitwise rotation on the binary pattern and calculates the corresponding decimal values. Finally, the minimal decimal value is retained as the rotation-invariant LBP code for the central pixel. Nevertheless, the discrimination of such LBP features is still limited for defect detection. As presented in Fig. 2(a), though the intensities of the defective region (P_1) and the background (P_3) are strikingly different, the LBP codes computed at P_1 and P_3 are likely to be indistinguishable. This is because the central pixel and its neighbors have similar gray values in a small radius. Since LBP reflects local variations of pixels, only the codes generated at the boundary of the defect (P_2) are expected to be remarkably different from that of background pixels. As shown in Fig. 2(b), if we set a large radius for LBP operator, P_1 and its surroundings will have different intensities and hence P_1 can be identified. But in such cases, the background pixels like P_3 may be compared with the defective pixels, which can make the faultless background stand out.

Fig. 2(c) provides an illustration of our proposed LBP-inspired feature extractor, which intends to measure variations

of pixels in horizontal, vertical, and two diagonal directions. In each direction, every pixel will be compared with T randomly selected anchor pixels and the comparison rule is same as the one used in LBP. We might as well take the vertical direction as an example. Once T anchor points are determined, all pixels in the same direction line will be compared with them. In short, each pixel will be described by four values, which correspond to four directions and spontaneously constitute a four-dimensional (4-D) feature. Since LBP-inspired feature extractor characterizes each pixel with pixels at various distances from different directions, features extracted by it can enjoy better visual discrimination. In subsequent implementations, T is uniformly set to eight.

Notice that most of the industrial images are captured in gray-scale format, which means that gray-level information can act as a reliable feature to distinguish defects from dynamic background. In light of this, we also compute a three-dimensional (3-D) intensity-based feature [3]. In addition, defects in surface images are with diverse shapes and patterns, and thus an eight-dimensional (8-D) texton feature [22] is employed for its advantage in texture classification [23]. Therefore, a total of fifteen-dimensional (15-D) statistical features that are computationally efficient and able to characterize pixel variations are selected in this paper, that is, each pixel in image I is characterized by a feature vector $f_i \in R^d, d = 15$.

C. Superpixel Segmentation

After image preprocessing and feature extraction, the image is then partitioned into compact and perceptually homogeneous superpixels. The reason for this procedure lies in two aspects. Since the number of superpixels in an image is far smaller than that of pixels, taking the superpixel as the smallest processing unit is expected to ease the computational burden to a certain degree. More importantly, some defects may occupy contiguous areas and no longer be consistent with the sparsity assumption in the pixel level. When a defect image is segmented into superpixels, there are only few superpixels that correspond to defects.

Therefore, superpixel segmentation actually enables entity sparsity pursuit (ESP) of defects.

Considering its high computation efficiency and boundary adherence property, SLIC algorithm [24] is used to segment image I into a set of superpixels $\{sp_i | i = 1, \dots, N\}$, where N denotes the expected number of superpixels. For each superpixel sp_i , we define its feature representation by averaging all the feature vectors of the pixels contained in it, i.e.,

$$x_i = \frac{1}{N_{sp_i}} \sum_{p_j \in sp_i} f_j \quad (8)$$

where N_{sp_i} is the number of pixels within the superpixel sp_i . As shown in Fig. 2(d), even if a small number of pixels (red ellipse) are contaminated by noise, the feature representation computed by (8) can still basically reflect the nature of the superpixel. In other words, such a feature representation has the advantage of being insensitive to noise. To balance the contribution of different features, each dimension of the feature is then recalculated by max-min normalization. After that, all the feature vectors of the superpixels constitute the feature matrix X of image I , i.e.,

$$X = [x_1, \dots, x_N]. \quad (9)$$

From the foregoing, we can say that only few columns of X represent defects, and this observation is the main origin that we propose to detect surface defects via ESP. In addition, this property also serves as the motivation for mining intrinsic priors of defect images, which will be elaborated in the following section.

D. Intrinsic Prior Mining

In this section, we mine intrinsic priors of defect images. This can not only help to maintain a compact model with no need to utilize complex regularization terms, but also guide LRR to fully explore its potential in defect detection scenarios.

1) **Background Prior (BP) Mining:** Given an input image, the defect region usually accounts for a small fraction of the whole image. That is to say, most of superpixels are intact, and a randomly selected superpixel is more likely to be defect-free. This motivates us to mine a BP.

For an input image I with superpixel set $\{sp_i | i = 1, \dots, N\}$, we randomly choose c superpixels and denote their feature vectors as x'_1, \dots, x'_c . Then, the feature representation x_B for the flawless background can be simply estimated by

$$x_B = \frac{1}{c} \sum_{i=1}^c x'_i. \quad (10)$$

Notice that c can be determined accordingly by the number of superpixels, i.e., N , and we empirically set $c = 0.1 \times N$. For each superpixel sp_i , the BP is formulated as follows:

$$BP_i = \|x_i - x_B\|_2^2. \quad (11)$$

Clearly, BP measures the similarity between the superpixel and the estimated background. Noted that similar ideas have been reported in [13] and [25], but the BP and optimization model explored in this paper are quite different. Specifically, images in both [13] and [25] are divided into uniform-sized

patches rather than varisized superpixels. Moreover, no reference background is constructed in [25]. To facilitate the problem solving, Cao *et al.* replaced LRR with the least squares regression, which performs slightly worse than LRR [13].

2) **Local Prior (LP) Mining:** After segmenting the image into a set of superpixels, we can simultaneously obtain the adjacency information of each superpixel, which prompts us to mine an LP from the perspective of visual saliency. Generally, visual saliency can be regarded as a kind of perceptual awareness that makes some items (i.e., defects) stand out from their neighbors and attract our attention immediately. Considering that one defective superpixel differs from its surroundings in most cases, we calculate an LP for each superpixel sp_i by

$$LP_i = \frac{1}{SPN_{sp_i}} \sum_{j \in \mathcal{N}_{sp_i}} \|x_i - x_j\|_2^2 \quad (12)$$

where \mathcal{N}_{sp_i} denotes the index set of superpixels that are adjacent to sp_i , and SPN_{sp_i} represents the cardinality of \mathcal{N}_{sp_i} . As we can see, LP is inclined to reflect local variabilities of superpixels, that is, background superpixels are less likely to be highlighted, as they have similar feature representations.

It should be stressed that the abovementioned priors are not immutable. Depending on different inspection tasks, one can surely mine more kinds of priors, such as location prior and semantic prior. As can be found in the following section, we aim to provide a paradigm and regard priors as pluggable components to the designed model.

E. Entity Sparsity Pursuit

1) **Entity Sparsity Pursuit:** By mining intrinsic priors of defect images, we can partly extrapolate the probability of being defective for each superpixel. However, such estimation might be inaccurate because of noise disturbance and varisized segments. Thus, we regard such priors as a kind of guidance information. Different from conventional low-rank-based models [26], [27] using complicated regularization terms, we present a compact architecture that can smoothly incorporate priors of defect images. Particularly, ESP detects surface defects by solving the following optimization problem:

$$\begin{aligned} \min_{Z, E} \quad & \|Z\|_* + \lambda \|EW\|_{2,1} \\ \text{s.t.} \quad & X = XZ + E \end{aligned} \quad (13)$$

where $W = \text{diag}(w_1, \dots, w_N)$ is a diagonal matrix. Review that in (5), the residue matrix E is supposed to indicate the column-specific corruptions. In terms of defect detection, if the i th superpixel belongs to the background, then the i th column of E is hopeful to be a sparse vector, otherwise the opposite. Return to (13), if the superpixel sp_i is part of the background, we are expected to set a large w_i to suppress its magnitude. Conversely, a small w_i is preferred to manifest the defect. With the mined intrinsic priors, we can naturally define¹

$$w_i = \exp(- (BP_i \times LP_i)) \quad (14)$$

¹To reduce noise disturbance, one can simply threshold intrinsic priors using their standard deviations.

or

$$w_i = \exp(-(\text{BP}_i + \text{LP}_i)). \quad (15)$$

In principle, (14) requires that both BP and LP should simultaneously take effect, whereas (15) allows either BP or LP to function.

2) Optimization: To solve problem (13), we first introduce an auxiliary variable J and convert it to the following problem:

$$\begin{aligned} \min_{Z, E} \quad & \|J\|_* + \lambda \|EW\|_{2,1} \\ \text{s.t.} \quad & X = XZ + E, Z = J. \end{aligned} \quad (16)$$

Then, the alternating direction method (ADM) [28] is adopted to solve problem (16). It minimizes the following augmented Lagrangian function:

$$\begin{aligned} L = & \|J\|_* + \lambda \|EW\|_{2,1} \\ & + \text{tr}(Y_1^T (X - XZ - E) + Y_2^T (Z - J)) \\ & + \frac{\mu}{2} (\|X - XZ - E\|_F^2 + \|Z - J\|_F^2) \end{aligned} \quad (17)$$

where tr denotes the matrix trace, i.e., the sum of the diagonal elements, $\|\cdot\|_F$ is the Frobenius norm, which calculates the square root of the sum of squares of all elements in a matrix, Y_1 and Y_2 are the Lagrange multipliers, and $\mu > 0$ is a penalty parameter. At this point, the problem defined in (16) becomes unstrained. Thus, it can be minimized with respect to J , Z , and E by fixing the other variables, and then updating the multipliers Y_1 and Y_2 . The solution steps are summarized in Algorithm 1, in which the norm $\|\cdot\|_\infty$ computes the largest absolute value of all entries in a matrix.

Step 1. Updating J : According to [29], the subproblem has the closed solution by matrix shrinkage operator. For each $\mu > 0$ and $G = Z + \frac{1}{\mu} Y_2$ with the rank of X being r , the optimal solution can be described as

$$J = \mathcal{D}_{\frac{1}{\mu}}^\perp(G) = U \text{diag} \left[\left(\sigma_i - \frac{1}{\mu} \right)_+ \right] V^T \quad (18)$$

where t_+ is the positive part of t , namely, $t_+ = \max(0, t)$, $U\Sigma V^T$ is the singular value decomposition (SVD) of G with $\Sigma = \text{diag}(\{\sigma_i\}_{1 \leq i \leq r})$.

Step 2. Updating Z : Since every part of the subproblem is quadratic, we can take the derivative with respect to Z and set it to zero, which gives

$$Z = (X^T X + I_N)^{-1} \left(X^T (X - E) + J + \frac{1}{\mu} (X^T Y_1 - Y_2) \right) \quad (19)$$

where I_N denotes an identity matrix.

Step 3. Updating E : In this subproblem, there exists an $\ell_{2,1}$ norm, which poses difficulties for optimization. Equivalently, we rewrite it as

$$\begin{aligned} E = & \arg \min \lambda \|H\|_{2,1} + \text{tr}(Y_1^T (X - XZ - E)) \\ & + \frac{\mu}{2} \|X - XZ - E\|_F^2 \end{aligned} \quad (20)$$

Algorithm 1: Solving Problem (17) by ADM.

Input: Feature matrix X and parameter λ

Initialize: $Z = J = E = 0$, $Y_1 = Y_2 = 0$, $\mu = 10^{-6}$, $\mu_{\max} = 10^6$, $\varepsilon = 10^{-3}$, $\rho = 1.1$

Output: Z , E

While not converge **do**

1. Fix the others and update J by

$$J = \arg \min \frac{1}{\mu} \|J\|_* + \frac{1}{2} \left\| J - \left(Z + \frac{Y_2}{\mu} \right) \right\|_F^2$$

2. Fix the others and update Z by

$$\begin{aligned} Z = & \arg \min \text{tr}(Y_1^T (X - XZ - E) + Y_2^T (Z - J)) \\ & + \frac{\mu}{2} (\|X - XZ - E\|_F^2 + \|Z - J\|_F^2) \end{aligned}$$

3. Fix the others and update E by

$$\begin{aligned} E = & \arg \min \lambda \|EW\|_{2,1} + \text{tr}(Y_1^T (X - XZ - E)) \\ & + \frac{\mu}{2} \|X - XZ - E\|_F^2 \end{aligned}$$

4. Update two Lagrange multipliers by

$$\begin{aligned} Y_1 &= Y_1 + \mu (X - XZ - E) \\ Y_2 &= Y_2 + \mu (Z - J) \end{aligned}$$

5. Update the parameter μ by

$$\mu = \min(\rho\mu, \mu_{\max})$$

6. Check the convergence conditions

$$\|X - XZ - E\|_\infty < \varepsilon, \quad \|Z - J\|_\infty < \varepsilon$$

end while

where $H = EW$. According to [30], after differentiating it with respect to E and setting the derivative to zero, we have

$$\frac{\lambda}{\mu} Q E W^T W + E = P \quad (21)$$

where $P = X - XZ + \frac{1}{\mu} Y_1$ and $Q = \text{diag}(q_1, \dots, q_N)$ is a diagonal matrix with the i th diagonal element being²

$$q_i = \frac{1}{\|h_i\|_2} \quad (22)$$

where h_i represents the i th column of H . Then, we separately manipulate each column vector, and the i th column of E and P is denoted as e_i and p_i , respectively. Based on the proofs in [31], we prove that the i th column of E can be deduced as

$$e_i = \begin{cases} \left(1 - \frac{\lambda w_i}{\mu \|p_i\|_2}\right) p_i, & \text{if } \|p_i\|_2 > \frac{\lambda w_i}{\mu} \\ 0, & \text{otherwise} \end{cases} \quad (23)$$

Thus, we can update E in a columnwise manner.

²The situation of $h_i = 0$ will be considered separately. Please refer to [30] for more details.

F. Image Postprocessing

After convergence, let E^* be the optimal solution to problem (13). To measure the defect level of the superpixel sp_i , we only need to quantify the response of the i th column of E^* , i.e.,

$$s_i = \|E^*(:, i)\|_2 = \sqrt{\sum_j (E^*(j, i))^2}. \quad (24)$$

Apparently, a large s_i means that the superpixel sp_i has a high probability to be defective, otherwise the opposite. Here, we actually get a map that encodes defect levels of all superpixels. But for those images that contain defects with large areas, raw defect maps generated by ESP might be scattered, i.e., some background regions have large defect levels or surface flaws have small defect levels. To enhance consistency of defect maps of such images, one can deploy the strategy proposed in [32] to modify the defect level of each superpixel by its adjacent superpixels, i.e.,

$$s'_i = s_i + \alpha \sum_{j \in \mathcal{N}_{sp_i}} s_j \cdot \exp\left(-\|x_i - x_j\|_2^2\right) \quad (25)$$

where α is a weight to control the influence of neighbors on the current superpixel, which is set to 0.5 in our experiment. With the refined defect map, OTSU algorithm [33] is then adopted to perform defect segmentation. After discarding abnormal connected components, we finally obtain the binary detection result (DR).

IV. EXPERIMENTS

This section details the experimental settings and evaluates the performance of the proposed method on several public datasets. The proposed algorithm is implemented in MATLAB R2018a on a computer with an Intel 3.6 GHz CPU.

A. Data Description

To test the generalization capability of the proposed method, three real-world and one synthetic surface defect datasets are adopted and the details of these datasets are as follows.

1) **Magnetic Tile (MT) Blowhole Dataset [34]:** The MT blowhole dataset totally provides 115 surface defect images with pixelwise ground truth (GT). Images in this dataset are captured in different illumination conditions with arbitrary sizes. Meanwhile, most of these images contain a kind of rain-streak-like noise, whose removal usually relies on sophisticated models. Even more, there exists severe vignette effect in the corner of some images. In a word, all these distractions are beyond the scope of this paper that aims to detect surface defects in an unsupervised manner. Therefore, we crop the images in this dataset to make them only contain the most relevant defective regions. To be fair, all subsequent experiments are carried out and evaluated using the recropped images. Examples of defect images and corresponding GT are shown in Fig. 3.

2) **Rail Surface Discrete Defect (RSDD) Dataset [3]:** Images in the RSDD dataset are categorized into two types and provided with pixelwise GT. Specifically, Type-I RSDD dataset contains 67 images captured from express rails, and Type-II

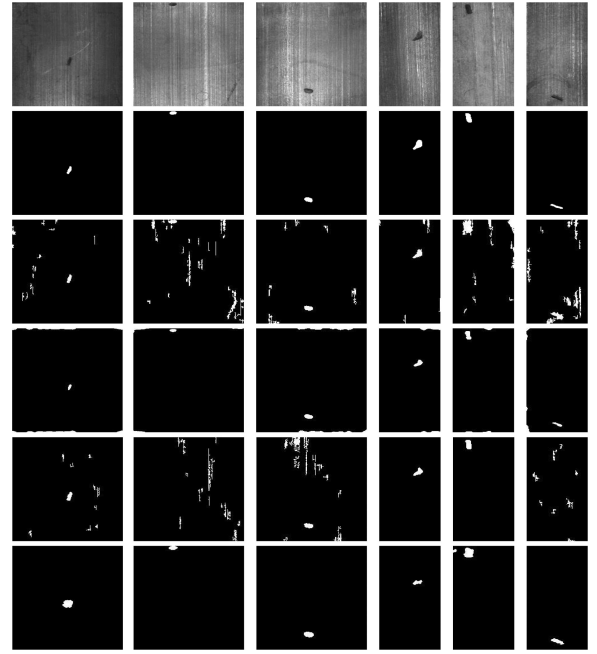


Fig. 3. Comparison of DRs on MT blowhole dataset. The original defect images and GT, the DRs obtained by contrast adjustment thresholding (CAT), saliency-based detection (SBD), smooth-sparse decomposition (SSD), and ESP are shown from top to bottom.

RSDD dataset contains 128 images captured from heavy haul rails. Images in Type-II dataset are narrower and have more consistent background than those in Type-I dataset, but defects contained in Type-II dataset are more sophisticated. Note that each image in this dataset contains at least one defect. Fig. 4 shows example defect images taken from the RSDD dataset.

3) **NEU Surface Defect Database [35]:** It consists of 300 defective images per class of hot-rolled steel strip with bounding box annotations. For the convenience of evaluation, we select the surface defect images of type patch, whose pixelwise GT is provided in [27]. Specially, due to the effect of disturbing factors, images of hot-rolled plates have heterogeneous defects and cluttered background with a low signal-to-noise ratio (SNR). All these characteristics make it far more challenging for surface defect inspection. Sample images and corresponding GT are visualized in Fig. 5.

4) **Synthetic Defect Dataset:** According to the practice in [25], we synthesize 30 noisy defect images for performance evaluation. Concretely, the textured background is corrupted with multiple circles and squares of arbitrary sizes. To make the synthetic images as realistic as possible, salt-and-pepper noise is introduced to the generated defective regions. Then, additive Gaussian noise with SNR between 10 and 50 dB is added to the full image. Sample images and corresponding GT in this dataset can be found in Fig. 6.

B. Comparison Methods

The experiments compare ESP with three state-of-the-art methods, including CAT [36], SBD [37], and SSD [38]. It must be said that all these three popular approaches do not specify

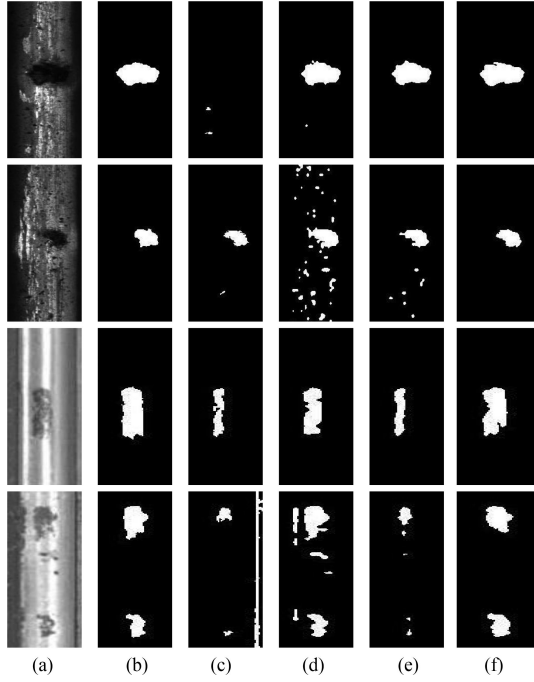


Fig. 4. Comparison of DRs. The first two rows illustrate the results for Type-I RSDD dataset. For visualization, images for Type-II RSDD dataset are widened and shown in the last two rows. (a) Original image. (b) GT. (c) CAT. (d) SBD. (e) SSD. (f) ESP.

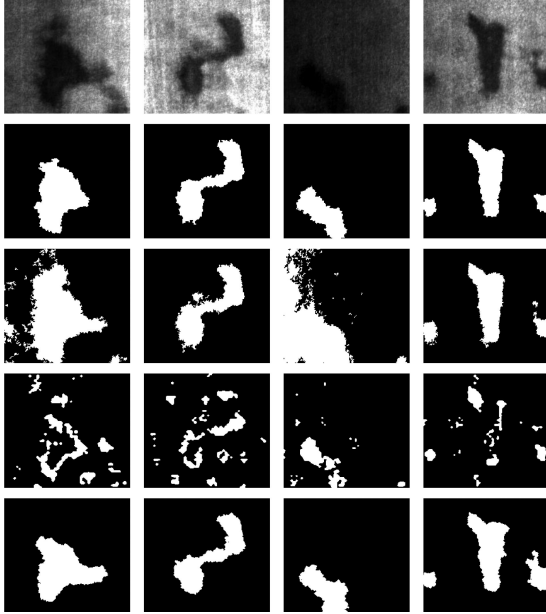


Fig. 5. Comparison of DRs on images of hot-rolled plates. The original defect images and GT, the DRs obtained by CAT, SSD, and ESP are shown from top to bottom.

redundant constraints and are almost generic. Other than the necessary postprocessing, all DRs are obtained with their default parameter settings.

C. Evaluation Metrics

As suggested in SSD method [38], false positive rate (FPR) and false negative rate (FNR) are calculated for performance

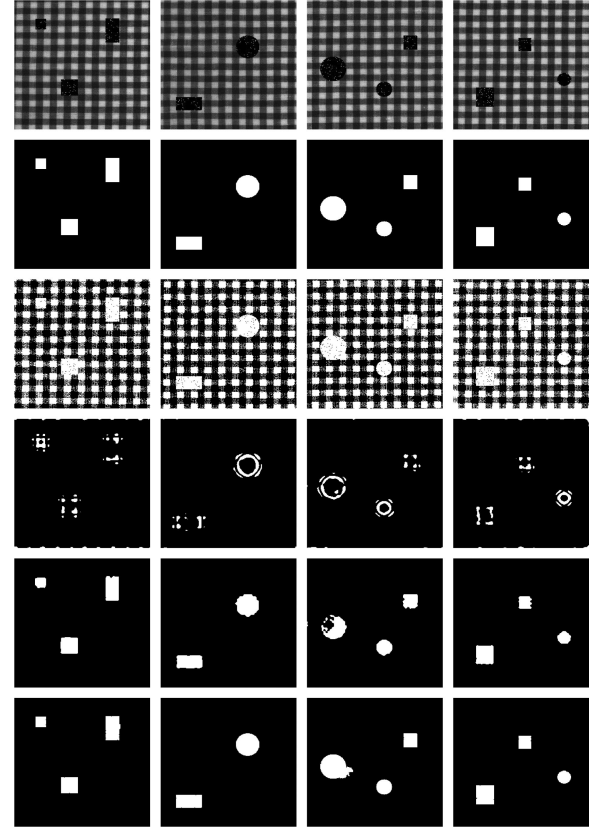


Fig. 6. Comparison of DRs on synthetic defect images. The original synthetic defect images and GT, the DRs obtained by CAT, SBD, SSD, and ESP are shown from top to bottom.

evaluation. FPR and FNR are defined as follows:

$$\text{FPR} = \frac{\text{FP}}{\text{FP} + \text{TN}}, \quad \text{FNR} = \frac{\text{FN}}{\text{FN} + \text{TP}} \quad (26)$$

where FP denotes the number of pixels that is falsely marked as defects, TN is the number of true background pixels, FN represents the number of undetected defect pixels, and TP indicates the number of correctly detected defect pixels. Namely, FPR is defined as the proportion of intact pixels that are falsely detected as defects, and FNR measures the percentage of defective pixels that are wrongly predicted as background. Besides, we also calculate the mean absolute error (MAE) to measure the difference between the DR and GT by

$$\text{MAE} = \frac{1}{\text{RN} \times \text{CN}} \sum_{i=1}^{\text{RN}} \sum_{j=1}^{\text{CN}} |\text{DR}(i, j) - \text{GT}(i, j)| \quad (27)$$

where RN and CN denote the row number and column number of the image, respectively. Obviously, the lower the values of FPR, FNR, and MAE, the closer the result is to human judgment.

D. Results and Analysis

1) *DRs of MT Blowhole Dataset*: Considering that there exist many microdefects in MT surface and images in the dataset are with various sizes, we experimentally select a large superpixel number, i.e., $N = 260$.

TABLE I

QUANTITATIVE COMPARISONS OF DIFFERENT DETECTION METHODS FOR MT BLOWHOLE DATASET

Dataset	Method	FPR	FNR	MAE
MT Blowhole Dataset	CAT	0.022	0.304	0.023
	SBD	0.007	0.487	0.009
	SSD	0.017	0.445	0.018
	ESP	0.004	0.229	0.004

TABLE II

QUANTITATIVE COMPARISONS OF DIFFERENT DETECTION METHODS FOR RSDD DATASET

Dataset	Method	FPR	FNR	MAE
Type-I RSDD Dataset	CAT	0.010	0.379	0.012
	SBD	0.004	0.312	0.007
	SSD	0.016	0.200	0.017
	ESP	0.006	0.283	0.008
Type-II RSDD Dataset	CAT	0.006	0.470	0.010
	SBD	0.003	0.444	0.008
	SSD	0.005	0.266	0.007
	ESP	0.004	0.218	0.006

Fig. 3 visualizes some defect images selected from MT blowhole dataset and the corresponding inspection results. It can be observed that although both CAT and SSD can locate defects, they are easy to produce false positives. In the frequency domain, the spectral magnitude of images tends to fall off at high frequencies. By normalizing the Fourier transformation of an image using the corresponding magnitude, SBD essentially removes all regular patterns. As shown in the fourth row of Fig. 3, SBD can effectively accommodate small surface variations, but tends to mistake parts of image borders as defects. Since ESP takes the superpixel as the essential element, it can restrain the influence of the noise and thus yield satisfactory DRs. The quantitative results are listed in Table I, which demonstrates that ESP enjoys the optimal overall performance.

2) *DRs of RSDD Dataset*: For Type-I RSDD dataset, the superpixel number N is empirically set to 160. As mentioned previously, images in Type-II RSDD dataset are narrower but with more sophisticated defects. Therefore, we use the same number to ensure a fine-grained segmentation for Type-II RSDD dataset.

DRs of several RSDD images are compared visually in Fig. 4, and the quantitative comparisons are listed in Table II. It can be found that SBD, SSD, and ESP are basically able to locate rail surface defects in most cases. As for the CAT method, it aims to create a gray-level mapping to enhance contrast of images. When the defect is cluttered with the image background, it fails to prevent missing detection. In contrast, SBD is inclined to detect defects in a more conservative manner, since it uses the phase to filter nonlocalized patterns and is sensitive to regions with abrupt changes. Numerically, SSD has the minimal false negatives for Type-I RSDD dataset, whereas ESP achieves fairly balanced performance for the whole dataset. As images in one dataset are segmented to the same number of superpixels, datasets containing images with similar-sized defects are more likely to yield satisfactory DRs. As mentioned earlier, defects in Type-II RSDD dataset are indeed more sophisticated, but their

TABLE III

QUANTITATIVE COMPARISONS OF DIFFERENT DETECTION METHODS FOR NEU SURFACE DEFECT DATABASE

Dataset	Method	FPR	FNR	MAE
NEU Surface Defect Database	CAT	0.116	0.030	0.105
	SSD	0.041	0.677	0.200
	ESP	0.088	0.266	0.143

TABLE IV

QUANTITATIVE COMPARISONS OF DIFFERENT DETECTION METHODS FOR SYNTHETIC DEFECT DATASET

Dataset	Method	FPR	FNR	MAE
Synthetic Defect Dataset	CAT	0.404	0.026	0.387
	SBD	0.007	0.571	0.035
	SSD	0.040	0.130	0.046
	ESP	0.001	0.002	0.001

sizes are relatively uniform. Therefore, ESP performs slightly better on Type-II RSDD dataset than on Type-I RSDD dataset.

3) *DRs of NEU Surface Defect Database*: The size of each surface defect image in this dataset is 200×200 and we experimentally set $N = 40$.

Fig. 5 shows comparative inspection results, for example, defect images of hot-rolled plates. Large flaw size is one of the major characteristics of this dataset, and it makes SBD fail to detect these defects, which are treated as regular subpatterns and removed by the phase-only transform. As listed in Table III, SSD achieves the lowest FPR but has the highest FNR, which indicates that SSD is prone to produce incomplete DRs, as shown in the fourth row of Fig. 5. It can be seen that both CAT and ESP provide promising DRs. Quantitatively, CAT possesses lower FNR and MAE, whereas ESP enjoys smaller FPR. Just as illustrated in the third column of Fig. 5, ESP is less likely to generate pseudodefects.

4) *DRs of Synthetic Defect Dataset*: The size of each image in this dataset is 256×256 ; thus, we segment them into a small number of superpixels and set $N = 50$.

Fig. 6 shows samples of DRs by all testing methods. Owing to neglecting the structural information, CAT is unable to effectively distinguish defects from the box patterns embedded in the image. Based on spectral analysis, SBD successfully removes the periodic patterns, but only the border of the defect is retained. SSD shows comparable detection performance to our method, since it exploits regularized high-dimensional regression to separate anomalous regions. Under the framework of LRR, one defect image is regarded as compositions of texture primitives, making the rare structural defect can still be identified by ESP. The average numerical DRs of comparison methods are listed in Table IV, which verifies that ESP outperforms the state-of-the-art methods.

E. Parameter Analysis

The tradeoff parameter λ in ESP directly regulates the sparsity of the residue matrix and thus has a notable impact on the DR. As shown in Fig. 7, while λ is ranging from 0.1 to 0.9, curves of FPR, FNR, and MAE are with little fluctuations, which demonstrate that ESP is insensitive to parameter λ . Unlike the

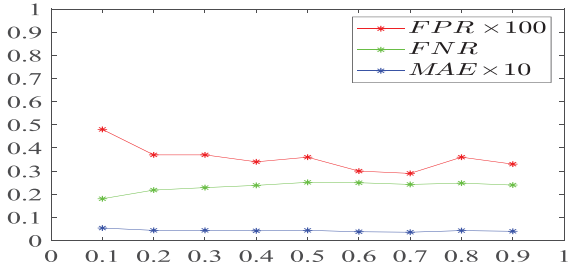


Fig. 7. Change curves of FPR, FNR, and MAE as a function of λ on the MT blowhole dataset.

TABLE V
RUNNING TIME OF ESP WITH VARYING NUMBER OF SUPERPIXELS

N	20	40	60	80	100	120	140	150	160	180	200
Time(s)	0.046	0.119	0.248	0.354	0.510	0.680	0.938	0.945	1.319	1.311	1.796

naive LRR in (5) that only utilizes λ to globally penalize the residue term, ESP also takes advantage of the intrinsic priors to locally control the magnitude of each column in the residue matrix, and this helps to interpret why ESP could work well under a range of parameter settings. Therefore, we set $\lambda = 0.3$ for all experiments.

F. Computational Complexity Analysis

We analyze the computational complexity of ESP denoted by $O(\cdot)$ notation that hides constant factors and smaller terms. Specifically, the major computation of Algorithm 1 stems from Step 1, which requires computing the SVD of an $N \times N$ matrix. At first glance, the complexity of ESP will be high if the number of superpixels is large. However, it should be noted that the feature matrix itself is used as the dictionary in ESP. According to the analysis in [18], the overall computational cost is at most $O(d^2N + d^3)$ provided that $d \leq N$, which obviously holds in our experiment ($d = 15$). This implies that ESP theoretically has linear complexity with respect to the number of superpixels.

Experimentally, we run an unoptimized version of ESP 100 times with N varying from 10 to 200. As illustrated in Table V, the average running time of ESP is less than 1 s when $N \leq 150$. On the whole, it can be efficient when the feature dimension d is not high. Nonetheless, a large number of superpixels will inevitably prolong the running time of ESP. Therefore, one can divide a large image into several square subimages and apply ESP to each subimage in parallel for surface defect inspection. In addition, the running speed can be further accelerated by introducing fast randomized SVD [39] or developing efficient implementations using high performance computing architectures [40], which also facilitate the proposed method for industrial applications.

V. CONCLUSION

This paper proposed an ESP method for surface defect detection. In terms of feature extraction, an intuitive LBP-inspired feature extractor was designed for industrial gray-scale images. As undamaged surface images generally show homogeneous

textures, which can be disrupted by defects that usually occupy small regions, we formalized the detection task as a low-rank and ESP problem. Instead of using complicated regularization terms, we presented a compact vision architecture, which can neatly integrate priors of defect images. Experimental results on three real-world and one synthetic defect datasets showed that our method had a reliable detection performance and enjoyed promising task generalization ability.

To detect surface defect at the entity level, ESP took the superpixel as the basic processing unit, but how to adaptively determine the number of superpixels was not discussed in this paper. In practice, the number of superpixels should be set according to the smallest defect size. In future research, we plan to put forward a multiscale segmentation based method, which is expected to automatically determine the number of superpixels to be segmented. On the other hand, we will explore more suitable binarization procedure such as hysteresis thresholding to improve the detection performance.

ACKNOWLEDGMENT

The authors would like to thank the Reviewers and Editors for their constructive comments to improve this paper. They would also like to thank Prof. H. Yan, Prof. W. Zou, Prof. G. Liu, Dr. S. Zhou, Dr. Y. Huang, and Dr. Q. Huangpeng for their selfless assistance or valuable suggestions.

REFERENCES

- [1] K. Liu, H. Wang, H. Chen, E. Qu, Y. Tian, and H. Sun, "Steel surface defect detection using a new Haar-Weibull-variance model in unsupervised manner," *IEEE Trans. Instrum. Meas.*, vol. 66, no. 10, pp. 2585–2596, Oct. 2017.
- [2] Y. Zhang, D. Lefebvre, and Q. Li, "Automatic detection of defects in tire radiographic images," *IEEE Trans. Autom. Sci. Eng.*, vol. 14, no. 3, pp. 1378–1386, Jul. 2017.
- [3] J. Gan, Q. Li, J. Wang, and H. Yu, "A hierarchical extractor-based visual rail surface inspection system," *IEEE Sensors J.*, vol. 17, no. 23, pp. 7935–7944, Dec. 2017.
- [4] D. Tsai, S. Wu, and W. Chiu, "Defect detection in solar modules using ICA basis images," *IEEE Trans. Ind. Inform.*, vol. 9, no. 1, pp. 122–131, Feb. 2013.
- [5] L. Bai, X. Yang, and H. Gao, "Corner point-based coarse-fine method for surface-mount component positioning," *IEEE Trans. Ind. Inform.*, vol. 14, no. 3, pp. 877–886, Mar. 2018.
- [6] H. Kong, J. Yang, and Z. Chen, "Accurate and efficient inspection of speckle and scratch defects on surfaces of planar products," *IEEE Trans. Ind. Inform.*, vol. 13, no. 4, pp. 1855–1865, Aug. 2017.
- [7] A. Kumar and G. K. H. Pang, "Defect detection in textured materials using optimized filters," *IEEE Trans. Syst., Man, Cybern. B, Cybern.*, vol. 32, no. 5, pp. 553–570, Oct. 2002.
- [8] X. Li, H. Jiang, and G. Yin, "Detection of surface crack defects on ferrite magnetic tile," *NDT & E Int.*, vol. 62, pp. 6–13, 2014.
- [9] M. R. Halfawy and J. Hengmehchai, "Automated defect detection in sewer closed circuit television images using histograms of oriented gradients and support vector machine," *Autom. Construction*, vol. 38, pp. 1–13, 2014.
- [10] J. K. Chandra and A. K. Datta, "Detection of defects in fabrics using subimage-based singular value decomposition," *J. Textile Inst.*, vol. 104, no. 3, pp. 295–304, 2013.
- [11] X. Xie and M. Mirmehdi, "TEXEMS: Texture exemplars for defect detection on random textured surfaces," *IEEE Trans. Pattern Anal. Mach. Intell.*, vol. 29, no. 8, pp. 1454–1464, Aug. 2007.
- [12] A. T. Bui and D. W. Apley, "A monitoring and diagnostic approach for stochastic textured surfaces," *Technometrics*, vol. 60, no. 1, pp. 1–13, 2018.
- [13] J. Cao, J. Zhang, Z. Wen, N. Wang, and X. Liu, "Fabric defect inspection using prior knowledge guided least squares regression," *Multimedia Tools Appl.*, vol. 76, no. 3, pp. 4141–4157, 2017.

- [14] F.-C. Chen and M. R. Jahanshahi, "NB-CNN: Deep learning-based crack detection using convolutional neural network and Naïve Bayes data fusion," *IEEE Trans. Ind. Electron.*, vol. 65, no. 5, pp. 4392–4400, May 2018.
- [15] J. Chen, Z. Liu, H. Wang, A. Núñez, and Z. Han, "Automatic defect detection of fasteners on the catenary support device using deep convolutional neural network," *IEEE Trans. Instrum. Meas.*, vol. 67, no. 2, pp. 257–269, Feb. 2018.
- [16] R. Ren, T. Hung, and K. C. Tan, "A generic deep-learning-based approach for automated surface inspection," *IEEE Trans. Cybern.*, vol. 48, no. 3, pp. 929–940, Mar. 2018.
- [17] E. Candès, X. Li, Y. Ma, and J. Wright, "Robust principal component analysis?" *J. ACM*, vol. 58, no. 3, pp. 1–37, 2011.
- [18] G. Liu, Z. Lin, S. Yan, J. Sun, Y. Yu, and Y. Ma, "Robust recovery of subspace structures by low-rank representation," *IEEE Trans. Pattern Anal. Mach. Intell.*, vol. 35, no. 1, pp. 171–184, Jan. 2013.
- [19] L. Zhuang *et al.*, "Constructing a nonnegative low-rank and sparse graph with data-adaptive features," *IEEE Trans. Image Process.*, vol. 24, no. 11, pp. 3717–28, Nov. 2015.
- [20] X. Shen and Y. Wu, "A unified approach to salient object detection via low rank matrix recovery," in *Proc. IEEE Conf. Comput. Vis. Pattern Recognit.*, 2012, pp. 853–860.
- [21] T. Ojala, M. Pietikäinen, and D. Harwood, "A comparative study of texture measures with classification based on featured distributions," *Pattern Recognit.*, vol. 29, no. 1, pp. 51–59, 1996.
- [22] M. Varma and A. Zisserman, "A statistical approach to texture classification from single images," *Int. J. Comput. Vis.*, vol. 62, no. 1/2, pp. 61–81, 2005.
- [23] J. Shotton, J. Winn, C. Rother, and A. Criminisi, "TextronBoost for image understanding: Multi-class object recognition and segmentation by jointly modeling texture, layout, and context," *Int. J. Comput. Vis.*, vol. 81, no. 1, pp. 2–23, 2009.
- [24] R. Achanta, A. Shaji, K. Smith, A. Lucchi, P. Fua, and S. Süsstrunk, "SLIC superpixels compared to state-of-the-art superpixel methods," *IEEE Trans. Pattern Anal. Mach. Intell.*, vol. 34, no. 11, pp. 2274–2282, Nov. 2012.
- [25] Q. Huangpeng, H. Zhang, X. Zeng, and W. Huang, "Automatic visual defect detection using texture prior and low-rank representation," *IEEE Access*, vol. 6, pp. 37965–37976, 2018.
- [26] H. Peng, B. Li, H. Ling, W. Hu, W. Xiong, and S. J. Maybank, "Salient object detection via structured matrix decomposition," *IEEE Trans. Pattern Anal. Mach. Intell.*, vol. 39, no. 4, pp. 818–832, Apr. 2017.
- [27] S. Zhou, S. Wu, H. Liu, Y. Lu, and N. Hu, "Double low-rank and sparse decomposition for surface defect segmentation of steel sheet," *Appl. Sci.*, vol. 8, no. 9, pp. 1–16, 2018.
- [28] Z. Lin, R. Liu, and Z. Su, "Linearized alternating direction method with adaptive penalty for low-rank representation," in *Proc. Adv. Neural Inf. Process. Syst.*, 2011, pp. 612–620.
- [29] J.-F. Cai, E. J. Candès, and Z. Shen, "A singular value thresholding algorithm for matrix completion," *SIAM J. Optim.*, vol. 20, no. 4, pp. 1956–1982, 2010.
- [30] F. Nie, H. Huang, X. Cai, and C. Ding, "Efficient and robust feature selection via joint $\ell_{2,1}$ -norms minimization," in *Proc. Adv. Neural Inf. Process. Syst.*, 2010, pp. 1813–1821.
- [31] J. Yang, W. Yin, Y. Zhang, and Y. Wang, "A fast algorithm for edge-preserving variational multichannel image restoration," *SIAM J. Imag. Sci.*, vol. 2, no. 2, pp. 569–592, 2011.
- [32] W. Zou, K. Kpalma, Z. Liu, and J. Ronsin, "Segmentation driven low-rank matrix recovery for saliency detection," in *Proc. 24th Brit. Mach. Vis. Conf.*, 2013, pp. 1–13.
- [33] N. Otsu, "A threshold selection method from gray-level histograms," *IEEE Trans. Syst., Man, Cybern.*, vol. SMC-9, no. 1, pp. 62–66, Jan. 1979.
- [34] Y. Huang, C. Qiu, and K. Yuan, "Surface defect saliency of magnetic tile," in *The Visual Computer*. New York, NY, USA: Springer, 2018, pp. 1–12.
- [35] K. Song and Y. Yan, "A noise robust method based on completed local binary patterns for hot-rolled steel strip surface defects," *Appl. Surf. Sci.*, vol. 285, pp. 858–864, 2013.
- [36] M. Win, A. Bushroa, M. Hassan, N. Hilman, and A. Ide-Ektessabi, "A contrast adjustment thresholding method for surface defect detection based on mesoscopy," *IEEE Trans. Ind. Inform.*, vol. 11, no. 3, pp. 642–649, Jun. 2015.
- [37] X. Bai, Y. Fang, W. Lin, L. Wang, and B.-F. Ju, "Saliency-based defect detection in industrial images by using phase spectrum," *IEEE Trans. Ind. Inform.*, vol. 10, no. 4, pp. 2135–2145, Nov. 2014.
- [38] H. Yan, K. Paynabar, and J. Shi, "Anomaly detection in images with smooth background via smooth-sparse decomposition," *Technometrics*, vol. 59, no. 1, pp. 102–114, 2017.
- [39] N. Halko, P.-G. Martinsson, and J. A. Tropp, "Finding structure with randomness: Probabilistic algorithms for constructing approximate matrix decompositions," *SIAM Rev.*, vol. 53, no. 2, pp. 217–288, 2011.
- [40] Y. Xu, Z. Wu, J. Li, A. Plaza, and Z. Wei, "Anomaly detection in hyperspectral images based on low-rank and sparse representation," *IEEE Trans. Geosci. Remote Sens.*, vol. 54, no. 4, pp. 1990–2000, Apr. 2016.



Jianzhu Wang received the B.Sc. degree in mathematics and applied mathematics from Shandong Agricultural University, Tai'an, China, in 2015. He is currently working toward the Ph.D. degree in computer science and technology with the School of Computer and Information Technology, Beijing Jiaotong University, Beijing, China.

His research interests include computer vision and pattern recognition.



Qingyong Li (M'09) received the B.Sc. degree in computer science and technology from Wuhan University, Wuhan, China, in 2001, and the Ph.D. degree in computer science and technology from the Institute of Computing Technology, Chinese Academy of Sciences, Beijing, China, in 2006.

He is currently a Professor with the Department of Computer Engineering, School of Computer and Information Technology, Beijing Jiaotong University, Beijing, China. His research

interests include computer vision and machine learning.



Jinrui Gan received the Ph.D. degree in computer science and technology from Beijing Jiaotong University, Beijing, China, in 2019.

He is currently an Engineer with the Global Energy Interconnection Research Institute Company, Ltd., Beijing, China. His research interests include computer vision and machine learning.



Haomin Yu received the B.Sc. degree in Internet of Things engineering from Anhui Normal University, Wuhu, China, in 2016. She is currently working toward the Ph.D. degree in computer science and technology with the School of Computer and Information Technology, Beijing Jiaotong University, Beijing, China.

Her research interests include machine learning and computer vision.



Xi Yang received the Ph.D. degree in traffic information engineering and control from Central South University, Changsha, China, in 2007.

She is currently an Associate Professor and Master Supervisor with the Department of Computer Technology and Internet of Things Engineering, School of Information, Beijing Wuzi University, Beijing, China. As a leading author, she has authored or coauthored 13 monographs and more than 30 peer-reviewed papers, and holds more than 20 patents. Her research inter-

ests include Internet of Things, wireless sensor network, and logistical information technology.